A SPECTRAL ANALYSIS MODAL METHOD APPLIED TO CAVITY FLOW OSCILLATIONS

Yang Zhang, Louis Cattafesta
Florida Center for Advanced Aero-Propulsion, Department of Mechanical Engineering
Florida State University
Tallahassee, FL
email: yz12b@my.fsu.edu

Lawrence Ukeiley
Department of Mechanical and Aerospace Engineering
University of Florida
Gainesville, FL

ABSTRACT

This paper presents a spectral analysis modal method applied to a canonical cavity flow at Mach 0.6. In particular, time-resolved (TR) unsteady surface pressure measurements are synchronized with non-time resolved (NTR) planar Particle Image Velocity measurements along the cavity midplane. We present a linear multiple-input/multiple-output (MIMO) frequency-domain model to estimate the cavity flow system. The model is further used for modal decomposition via Proper Orthogonal Decomposition (POD) in the spectral domain. Temporally and spatially coherent structures associated with Rossiter modes are identified. These results are compared with corresponding POD and Dynamic Mode Decomposition (DMD) modes obtained using independent time-resolved PIV measurements, which show strong similarities in the resulting modes.

INTRODUCTION

Proper Orthogonal Decomposition (POD) (Lumley, 1967), dynamic mode decomposition (DMD) (Schmid *et al.*, 2010), and resolvent analysis (McKeon & Sharma, 2010) are popular modal analysis tools that provide fundamental understanding and knowledge of turbulent flows, for example to identify coherent structures (Berkooz *et al.*, 1993), develop a reduced-order model (Pinnau, 2008), or facilitate flow control. Snapshot POD (Sirovich, 1987) uses instantaneous independent snapshots of the flow at different time instances to decompose a flow field into spatially orthonormal modes. The velocity field at the times corresponding to those of the snapshots can then be reconstructed using a linear combination of time-dependent POD coefficients and the spatial modes.

Note that this version of POD only guarantees spatially coherent structures, but the temporal dynamics of the flow field is not captured without time-resolved data. While feasible in simulations, time-resolved data remain beyond the reach of most current experiments due to either the high cost and/or limitations of current instrumentation. The velocity field is generally available at a sub-Nyquist rate (~ 15 Hz), while data at discrete locations (e.g., wall pressure) are available at time-resolved rates. Hence, current state-of-the-art experiments often employ variants of stochastic estimation (Adrian, 1979) to estimate the velocity field given statistical information about its relationship to surface pressure. Modified Stochastic Estimation combines stochastic estimation with POD to estimate the POD temporal coefficients rather than velocity field itself. A Fourier Transform provides a frequency domain or spectral version (Tinney *et al.*, 2006). Deficiencies of these stochastic estimation approaches include sensitivity to noise and overfitting (due to a large number of parameters in the estimation). Hence, current stochastic estimation approaches fall short of what is required to obtain a model that is generally suitable for appropriate application of modern modal analysis tools, such as DMD and resolvent analysis.

The current approach, termed "spectral analysis modal method (SAMM)" links Spectral LSE from Tinney *et al.* (2006) with a Multi-Input/Multi-Output (MIMO) system based model to circumvent these problems. SAMM possesses a striking resemblance to the ideas proposed by Lumley concerning the original POD, and recently Towne *et al.* (2018) presented an efficient algorithm for applications of the POD in the frequency domain yielding frequency dependent modes. It should be noted that as originally shown by Lumley (1967) and George (1988), the POD reduces to harmonic analysis over directions which are stationary (i.e., time); hence applying the POD in the frequency domain is the proper application when appropriate data are available. This method exploits our ability to measure the auto- and cross-correlation functions between spatially (but not time resolved) flow field data and time- (but not spatially) resolved surface pressure data. Here, we transform these measured functions to the frequency domain using the Discrete Fourier Transform (DFT) and employ MIMO conditional spectral analysis methods to construct measured transfer and coherence functions. The temporally- and spatially coherent structures are identified by applying spectral POD and are compared with the ones obtained from independent time-resolved measurements obtained subsequently with TR-Particle Image Velocimetry (PIV). In the current study, a canonical cavity flow at Mach 0.6, which exhibits strong

self-sustaining velocity/pressure oscillations, is our targeted flow and is used to demonstrate the relationship between the modal shapes detected by different methods in this flow field. The primary contribution of this work is a procedure to perform POD in the spectral domain without time-resolved velocity field measurements.

METHODOLOGIES
Experimental Setup
The experiments consist of two parts: the first part is for SAMM and the second part is time-resolved measurements for validation purpose. The details of the first experimental setup can be found in (Zhang *et al.*, 2017); therefore, it is only briefly summarized here. Two-component Particle Image Velocimetry (PIV) is performed to obtain the streamwise flow field on center plane of a cavity with $L/D = 6$ and $W/D = 3.85$. A schematic of the setup is provided in Figure 1b. A double-pulse Evergreen Nd:YAG laser (EVG00200) produces laser pulses at a repetition rate of 15 Hz. The cavity model is instrumented with $M = 10$ Kulite unsteady pressure transducers (Figure 1a). For fluctuating surface pressure measurements, the data are acquired at the maximum acquisition rate of 204.8 kHz for 15 seconds per PIV run. The resulting vector resolution is 2.8 vectors/mm.
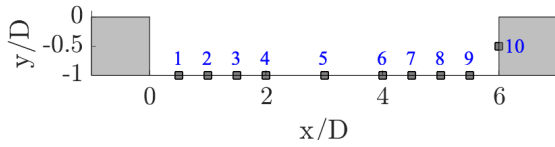
(a) Location of unsteady pressure sensors
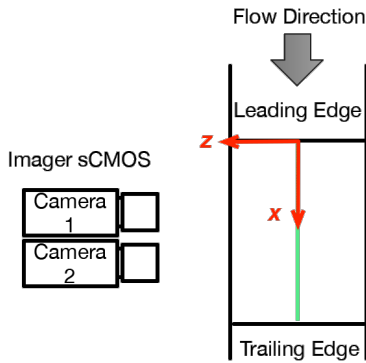
(b) Schematic of 2 component PIV setup (not to scale)

Figure 1: Schematics of experimental setup.

The time-resolved PIV measurements are achieved by by a Photonix DM dual-head laser and a Phantom V2012 high speed camera. A 105mm f2.8 Nikon lens with a 532 nm band-pass filter is used in this case. The sampling rate is 16 kHz with an image resolution of 1280×464 pixels, and a total number of 16000 image pairs are acquired. A 96×96 to 32×32 pixels multi-pass scheme with a 75% overlap is used to calculate the velocity field, resulting in a vector resolution of approximately 1 vector/mm. All the PIV images are acquired and processed using DaVis software 8.4. Multivariate outlier detection (MVOD) (Griffin *et al.*, 2010)

is used as the final post-processing step. The TR-PIV measurements are also performed at other frequencies, i.e., 8 kHz and 20 kHz, no aliasing on the Rossiter modes Rossiter (1964) are observed.

Multi-Input/Multi-Output System
The flow field is modeled by a MIMO system. In the current work, the fluctuating surface pressure at different locations are considered as the inputs, while the 2-D velocity field is the output as shown in Figure 2. The resulting velocity field is a summation of the contributions from all inputs (pressure).
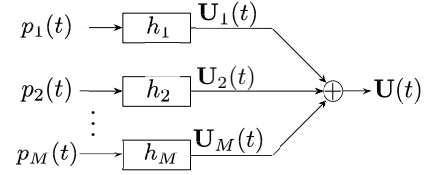

Figure 2: MIMO system

By performing a Fourier transform, the MIMO system is expressed in the frequency domain

$$\mathbf{U}(f) = \sum_{i=1}^{M} H_i(f) P_i(f), \tag{1}$$

where i is the sensor index. However, the transfer function $H_i(f)$ is not known without time-resolved velocity data, so $\mathbf{U}(f)$ cannot be calculated.

An alternative approach is as follows

$$P_j^*(f)\mathbf{U}(f) = \sum_{i=1}^{M} H_i(f) P_j^*(f) P_i(f), \tag{2}$$

$$\frac{2}{T} E[P_j^*(f)\mathbf{U}(f)] = \sum_{i=1}^{M} H_i(f) \frac{2}{T} E[P_j^*(f) P_i(f)], \tag{3}$$

$$G_{p_j\mathbf{U}}(f) = \sum_{i=1}^{M} H_i(f) G_{p_j p_i}(f), \tag{4}$$

where $*$ represents complex conjugate, $G_{p_j\mathbf{U}}$ is the cross-spectrum between pressure and velocity, $G_{p_j p_i}$ is the auo/cross-spectrum matrix of pressure. However, the equation above still cannot be used directly without time-resolved data. Noting that the cross-correlation and cross-spectrum are Fourier-transform pairs,

$$G_{xy}(f) = \int_{-\infty}^{+\infty} R_{xy}(\tau) e^{-j2\pi f\tau} d\tau, \tag{5}$$

where R_{xy} is the cross-correlation between fluctuating surface pressure and the velocity and can be calculated using non-time-resolved data by shifting the time-delay. It should be noted that this methodology is essentially equivalent to the Spectral LSE proposed by Tinney *et al.* (2006).

The cross-correlation R_{pu} is defined as

$$R_{pu}(\tau) = \int_{-\infty}^{+\infty} p(t) u(t+\tau) d\tau. \tag{6}$$

However, since $u(t + \tau)$ is not known, a time shift modifies this equation to an equivalent form

$$R_{pu}(\tau) = \int_{-\infty}^{+\infty} p(t - \tau)u(t)d\tau. \tag{7}$$

Similarly,

$$R_{P_i P_j}(\tau) = \int_{-\infty}^{+\infty} p_i(t)p_j(t + \tau)d\tau. \tag{8}$$

Then the cross-spectrum is estimated using a discretized form of a finite Fourier transform T

$$G_{xy}(f) = \int_{-T/2}^{+T/2} wR_{xy}(\tau)e^{-j2\pi f\tau}d\tau. \tag{9}$$

where w is a window function. Finally, the transfer functions H_i are obtained by solving Equation 4 in the matrix form.

POD Algorithm

We use the Spectral POD algorithm documented in (Towne *et al.*, 2018), which is briefly summarized here.

1. For each data block $n = 1, 2, \ldots, N_b$, assemble the data matrix $Q^{(n)} = [q_1^{(n)}, q_2^{(n)}, \cdots, q_{N_f}^{(n)}]$, where $q_k^{(n)}$ represents a snapshot and N_f is the number of snapshots in each block.
2. Then using a (windowed) fast Fourier transform, calculate and store the row-wise DFT as $\hat{Q}^{(n)} = $ FFT$(Q^{(n)}) = [\hat{q}_1^{(n)}, \hat{q}_2^{(n)}, \ldots, \hat{q}_{N_\omega}^{(n)}]$. The column $\hat{q}_k^{(n)}$ contains the nth realization of the Fourier mode at the kth discrete frequency f_k.
3. Assemble a new matrix $\hat{Q}_{f_k} \leftarrow [\hat{q}_k^{(1)}, \hat{q}_k^{(2)}, \ldots, \hat{q}_k^{(N_b)}]$ for each frequency $k = 1, 2, \ldots, N_f$ (or at frequencies of interest).
4. Calculate the matrix $M_{f_k} \leftarrow \hat{Q}_{f_k}^* \hat{Q}_{f_k}$.
5. Perform an eigenvalue decomposition $M_{f_k} = \Theta_{f_k}\tilde{\Lambda}_{f_k}\Theta_{f_k}^*$.
6. Obtain the POD modes $\tilde{\Psi}_{f_k} = \hat{Q}_{f_k}\Theta_{f_k}\tilde{\Lambda}_{f_k}^{-1/2}$ and modal energies $\tilde{\Lambda}_{f_k}$ for the kth discrete frequency.

In the SAMM case, Step 1 is not needed, and the pressure data were down-sampled to 25600 Hz with $nfft = 2048$. $P_i(f)$ is calculated with a Hanning window per snapshot period ($-1024dt$ to $1024dt$), and $\mathbf{U}(f)$ is obtained from Equation 1 to form $\hat{Q}^{(n)}$ in Step 2. The total number of blocks is $N_b = 4772$ with no overlap. In the case of TR-PIV, the $nfft$ is set to 1280 with 75% overlap, which results in 47 blocks.

Dynamic Mode Decomposition

The DMD algorithm applied in the current study is based on the total-least-square DMD (TDMD) in Hemati *et al.* (2017), which is robust to measurement noise. The procedure is summarized here.

1. An operator A_{DMD} is defined as $A_{DMD} = YX^\dagger$, where X and Y are data matrices containing snapshots of flow that are separated by one sample interval $[z_1, z_2, \cdots, z_{m-1}]$ and $[z_2, z_3, \cdots, z_m]$, respectively, and $X^\dagger$ denotes the *Moore-Penrose pseudoinvese* of X.

2. Construct the augmented snapshot matrix $z := \begin{bmatrix} X \\ Y \end{bmatrix}$, compute the SVD of Z as $Z = USV^*$, and retain the first n columns of V, denoting them as V_n.
3. Project X and Y onto V_n basis, getting $\bar{X} = XV_n$ and $\bar{Y} = YV_n$.
4. Calculate the SVD of $\bar{X}$ as $\bar{X} = \bar{U}\bar{S}\bar{V}^*$.
5. To calculate the eigenvalues and eigenvectors of A_{DMD} more efficiently, A_{DMD} is projected onto the reduced POD basis as $\tilde{A}_{DMD} = \bar{U}^*\bar{Y}\bar{V}\bar{S}^{-1}$.
6. We compute the eigenvalues and eigenvectors of $\tilde{A}_{DMD}$ as $\tilde{A}_{DMD}\phi = \lambda\phi$.
7. The DMD mode corresponding to the DMD eigenvalue λ is then given by $\Phi = U\phi$
8. The growth rate of the mode is calculated from the eigenvalue λ as $g = \log|\lambda|f_s$, while the frequency is $f = \angle\lambda f_s/(2\pi)$, where f_s is the sampling frequency.

RESULTS

Although the auto/cross-coefficient between the pressure signals can be more accurately evaluated using the longer TR data, it is not beneficial in the current method. As shown in Figure 3, small differences exist between two methods. The one calculated from TR and NTR data uses less samples such that it is a subset of the more converged result calculated from TR data that have substantially more samples. This mismatch is natural due to the presence of noise in the measurements. Because the cross-correlation coefficient between pressure and velocity has to be calculated using TR and NTR data and noise existing in the measurements, using a more converged R for the pressure signals does not result in a better estimation of the transfer function $H(f)$ by using Equation 4. Empirically, we found it is better to calculate R_{pu} and R_{pp} in a consistent manner using TR and NTR data.
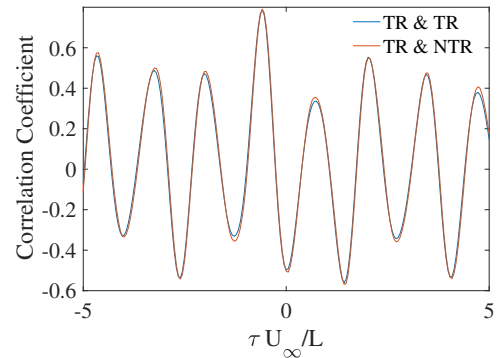

Figure 3: Cross-correlation between 1st and 10th pressure signals using different methods. TR & TR uses 30 million samples, and TR & NTR uses 4772 samples.

A typical plot corresponding to the cross-correlation between a local vertical velocity component near the trailing edge and the pressure signal on the aft wall is presented in Figure 4. The magnitude of the correlation decreases as the time delay increases or decreases. However, the coefficient never decays to zero due to the natural self-sustaining oscillations of the cavity flow. The correlation between local unsteady pressure and global velocity field are shown in Fig-

ure 5. Similar analysis at other other locations make it clear that the high correlation mainly exists along the shear layer across the cavity opening. Due to the acoustic feedback phenomenon in the cavity flow, the global cross-correlation between velocity and pressure at different locations present a similar wave pattern with a phase shift (time delay).
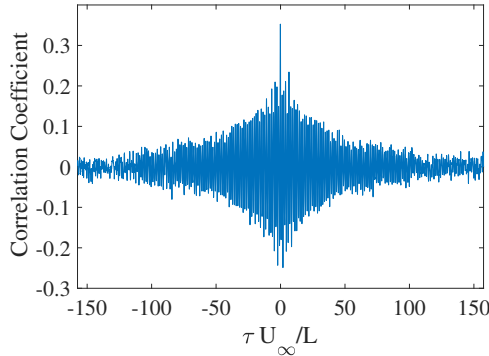

Figure 4: Cross-correlation between the local v component near the trailing edge ($x/D = 6$, $y/D = 0$) and pressure (10th sensor) on the aft wall.

(a) Sensor 1 ($x/D = 0.5, y/D = -1$)
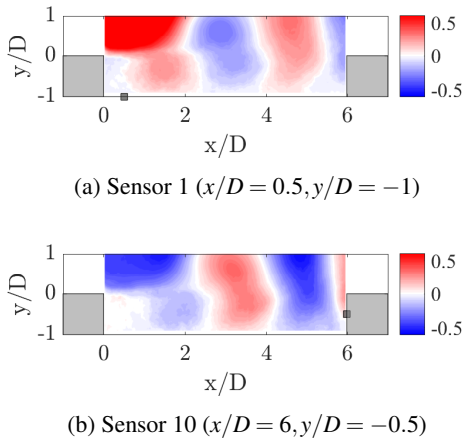

(b) Sensor 10 ($x/D = 6, y/D = -0.5$)

Figure 5: Global cross-correlation between the v velocity component and pressure for $\tau = 0$ at different locations. The black markers indicate the location of the pressure sensor.

As shown above, R oscillates, which introduces finite record length effects in the auto/cross spectral density calculation as the period T is necessarily truncated. The choice of T represents a compromise between frequency resolution and random uncertainty. An improper choice of df may also result in energy leakage. Because the main interests of the current study are the strong oscillations, i.e. Rossiter modes, a choice of $2048 dt$ is selected for T resulting in relatively smooth peaks with 12.5 Hz resolution in the spectrum as shown in Figure 6. The dominant Rossiter mode (2nd) shows a significantly higher amplitude compared with other modes and broadband fluctuations, which results in a more clear modal shape in the following discussion.
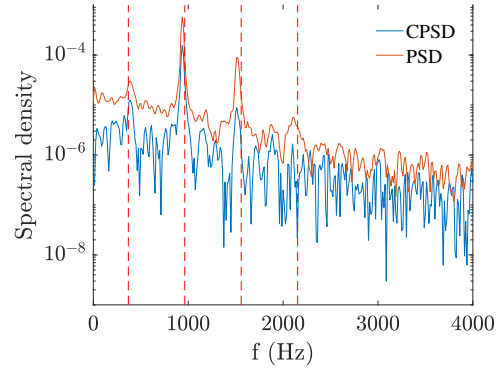

Figure 6: Cross-spectral density: between local v component near the trailing edge ($x/D = 6$, $y/D = 0$) and pressure (10th sensor) on the aft wall; Power spectral density: pressure from (10th sensor) on the aft wall. Dashed lines indicate Rossiter frequencies predicted by $St = \frac{fL}{U_\infty} = \frac{n-\alpha}{1/\kappa + Ma_\infty/\sqrt{1+(\gamma-1)Ma_\infty^2/2}}$ (Heller *et al.*, 1970).

By using SAMM and SPOD, the flow field dynamics of velocity seemingly lost in the NTR-PIV measurements are recovered via this linear model, and the dynamically important structures are extracted. The rank 1 modal shapes corresponding to the first four Rossiter frequencies obtained from SAMM and TR-PIV are compared in Figure 7. Both modal shapes of u and v exhibit strong wave patterns which are the characteristics of traveling waves. By comparing the modes obtained from SAMM to those from TR-PIV, we observe strong similarities for modes corresponding to Rossiter modes 2 to 4.

Unlike the spatial POD that distributes energy in the spatial orthonormal modes, the modes provided in Figures 7e and 7f correspond to a particular frequency. Because SAMM can only recover the energy in the velocity field that are linearly correlated with the pressure fluctuations, the total energy recovered is less than the original total energy. For Rossiter modes 2 and 3, the energy fraction of the rank 1 mode is approximately 93% and 91%, respectively, which is also related to the fact that the pressure fluctuations are dominant in the 2nd and 3rd Rossiter mode. Because the energy are coupled in velocity and pressure, they present the same energy signature. For Rossiter modes 1 and 4, the rank 2 mode has a non-negligible amplitude in Figure 7e. This explains why the two rank 1 mode shapes from SAMM do not match their respective counterparts from application of POD of the TR-PIV.

It is also clear that the 1st mode is not well resolved compared with other modes, which is due to two aspects. First, the amplitude of the velocity/pressure fluctuations are relatively small compared to the broadband fluctuations than for the 2nd and 3rd modes, which affects the signal-to-noise ratio. In addition, the NTR-PIV data contains less cycles of the 1st Rossiter mode compared with higher frequency modes. These results in increased level of uncertainty in the correlation between the velocity and pressure data. This can be potentially improved by increasing the number of NTR-PIV samples, although this increases experimental and computational cost. Second, T is 0.08 seconds, which affects the spectral resolution.

For the 2nd Rossiter mode, we observe that the mode shape is very similar to the cross-correlation map in Fig-

ure 5. This is because the level of pressure fluctuations of the 2nd mode has higher amplitude (dominant mode), which results in a stronger correlation between the velocity and pressure. Therefore, the correlation between velocity and pressure for other Rpssiter modes are all below that of the 2nd mode. With a high level of correlation, SAMM can easily recover the dynamics of the original flow field, i.e., 2nd and 3rd mode in the current study. Similarly, the 4th mode has a lower amplitude compared with other modes.

The original TR velocity fields were low-pass filtered at 8 kHz, and then TDMD was applied on 250 snapshots with a reduced rank of 80. The resulting DMD modes corresponding to the fist four Rossiter modes are provided in Figure 8, which exhibit strong similarities to the POD modes (Figuer 7). However, the modal shapes are not as clear as the POD modes at the same frequencies. DMD essentially seeks a linear approximation between the successive snapshots similar to SAMM albeit with less data. The oscillatory modes have periodic variations but broadband turbulent flows cannot be described by a single deterministic mode. Therefore, the linear mapping of the high level broadband turbulence introduces noise into the DMD modes. The POD modes present more clear structures because they are ensemble DMD modes that provide the optimal basis (Towne *et al.*, 2018). The modal shapes detected by these two methods are essentially the same time-spatial coherent structures in the flow field.

Conclusion

This paper presents an alternative method of spectral POD to recover the temporal dynamics in the NTR velocity field of a cavity flow at Mach 0.6 by using the information from TR fluctuating pressure and NTR velocity field. The transfer function is estimated between pressure and velocity, which is computed via DFT of auto/cross-correlation between pressure and velocity. Then the POD is used to identify the spatial-temporal coherent structures for the first 4 Rossiter modes in the cavity flow. Similar to linear stochastic estimation, good correlation between NTR and TR data is required to obtain the accurate transfer function between the inputs and outputs. SAMM recovers the high frequency ($\geq$ 2nd) modes well compared to the separate TR PIV measurements in the same cavity flow. SAMM is fundamentally limited by the linear correlation and, hence, signal-to-noise ratio of tonal to broadband turbulent fluctuations, which can be potentially improved by acquiring more data samples. POD and DMD essentially provide the same dynamically important spatial coherent modes of the flow field. However, the modal shapes are less clearly observed using DMD due to high level of broadband turbulence. Since TR-PIV is not always feasible, SAMM provides an attractive alternative method to time-domain LSE.

REFERENCES

Adrian, Ronald J. 1979 Conditional eddies in isotropic turbulence. *The Physics of Fluids* **22** (11), 2065–2070.

Berkooz, Gal, Holmes, Philip & Lumley, John L. 1993 The proper orthogonal decomposition in the analysis of turbulent flows. *Annual Review of Fluid Mechanics* **25** (1), 539–575.

George, William K. 1988 Insight into the dynamics of coherent structures from a proper orthogonal decomposition. In *Symposium on Near Wall Turbulence*. Dubrovnik, Yugoslavia.

Griffin, John, Schultz, Todd, Holman, Ryan, Ukeiley, Lawrence S. & Cattafesta, Louis N. 2010 Application of multivariate outlier detection to fluid velocity measurements. *Experiments in Fluids* **49** (1), 305–317.

Heller, H. H., Holmes, D. G. & Covert, E. E. 1970 Flow-induced pressure oscillations in shallow cavities AFFDL-TR-70-104.

Hemati, Maziar S., Rowley, Clarence W., Deem, Eric A. & Cattafesta, Louis N. 2017 De-biasing the dynamic mode decomposition for applied koopman spectral analysis of noisy datasets. *Theoretical and Computational Fluid Dynamics* **31** (4), 349–368.

Lumley, J. L. 1967 The structure of inhomogeneous turbulent flows. In *Atmospheric turbulence and radio propagation* (ed. A. M. Yaglom & V. I. Tatarski), pp. 166–178.

McKeon, B. J. & Sharma, A. S. 2010 A critical-layer framework for turbulent pipe flow. *Journal of Fluid Mechanics* **658**, 336–382.

Pinnau, René 2008 *Model Reduction via Proper Orthogonal Decomposition*, pp. 95–109. Berlin, Heidelberg: Springer Berlin Heidelberg.

Rossiter, J. E. 1964 Wind-tunnel Experiments on the Flow over Rectangular Cavities at Subsonic and Transonic speeds. *Tech. Rep..* Aeronautical Research Council Reports and Memoranda, no. 3438.

Schmid, P. J., Li, L., Juniper, M. P. & Pust, O. 2010 Applications of the dynamic mode decomposition. *Theoretical and Computational Fluid Dynamics* **25** (1), 249–259.

Sirovich, Lawrence 1987 Turbulence and the dynamics of coherent structures, part i-iii. *Quarterly of Applied Mathematics* **45** (3), 561–590.

Tinney, C. E., Coiffet, F., Delville, J., Hall, A. M., Jordan, P. & Glauser, M. N. 2006 On spectral linear stochastic estimation. *Experiments in Fluids* **41** (5), 763–775.

Towne, Aaron, Schmidt, Oliver T. & Colonius, Tim 2018 Spectral proper orthogonal decomposition and its relationship to dynamic mode decomposition and resolvent analysis. *Journal of Fluid Mechanics* **847**, 821–867.

Zhang, Yang, Cattafesta, Lou & Ukeiley, Lawrence 2017 Identification of coherent structures in cavity flows using stochastic estimation and dynamic mode decomposition. In *10th International Symposium on Turbulence and Shear Flow Phenomena (TSFP10)*. Chicago, USA.
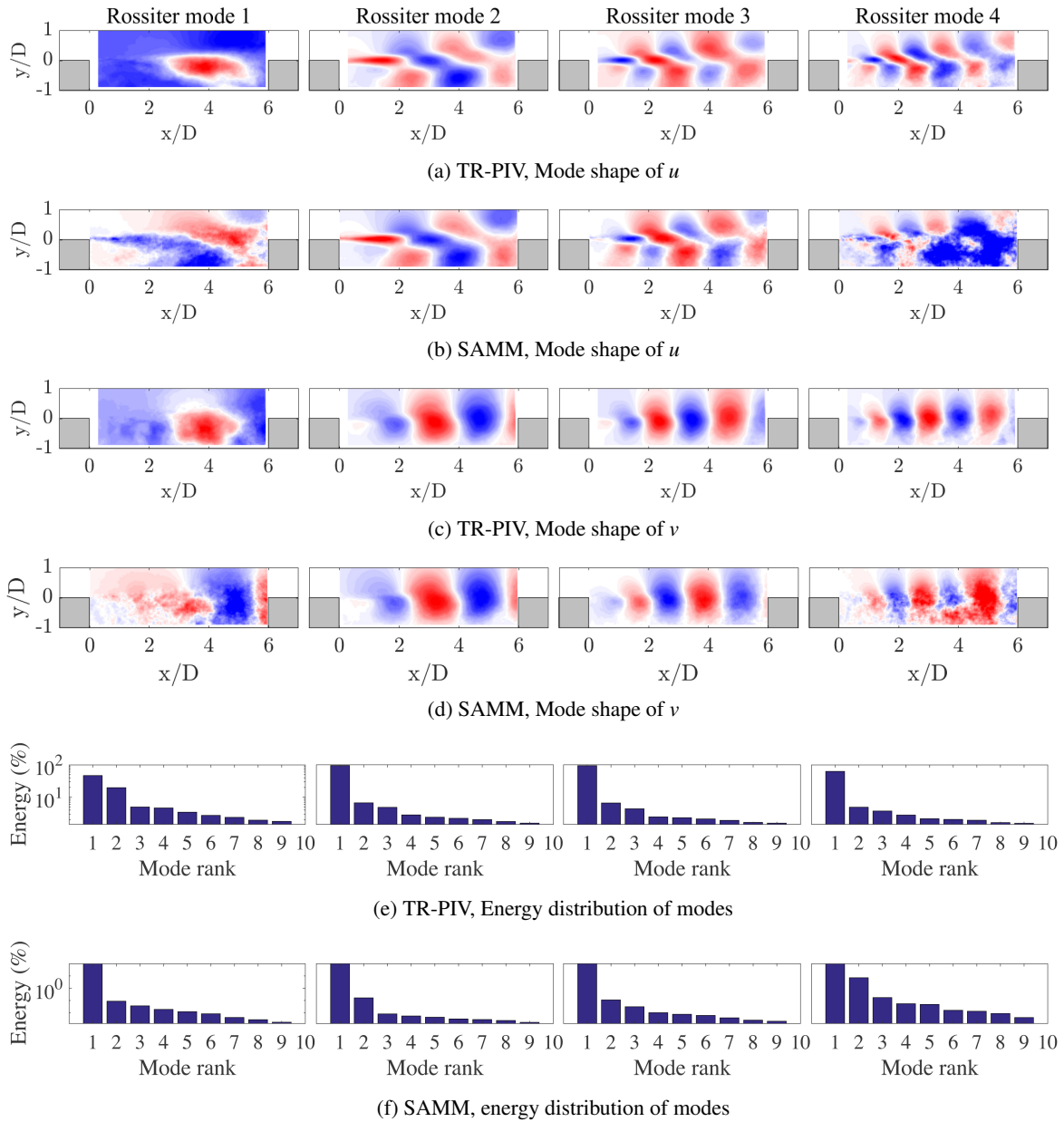
(a) TR-PIV, Mode shape of *u*

(b) SAMM, Mode shape of *u*

(c) TR-PIV, Mode shape of *v*

(d) SAMM, Mode shape of *v*

(e) TR-PIV, Energy distribution of modes

(f) SAMM, energy distribution of modes

Figure 7: POD modal shapes corresponding to the first 4 Rossiter modes.
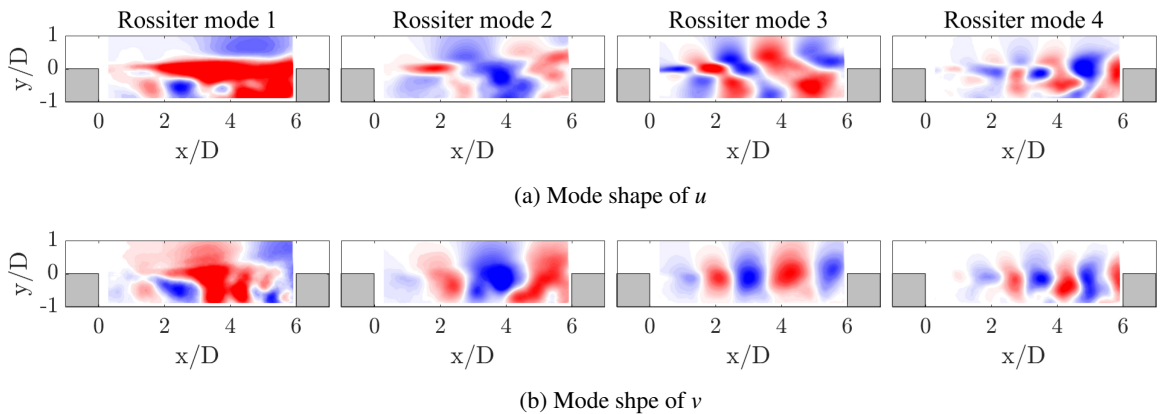

(a) Mode shape of *u*

(b) Mode shpe of *v*

Figure 8: TDMD modal shapes corresponding to the first 4 Rossiter modes.